Journal of Photopolymer Science and Technology
Volume 27, Number 3 (2014) 307–316 © 2014SPST

Review

Carrier Mobility in Organic Thin-film Transistors: Limiting Factors and Countermeasures

Masakazu Nakamura and Ryosuke Matsubara

Graduate School of Materials Science, Nara Institute of Science and Technology,
8916-5 Takayama, Ikoma, Nara 630-0192, Japan
mnakamura@ms.naist.jp

Device physics in organic thin-film transistors (OTFTs) have been extensively studied along with the efforts to improve device performance and to develop their applications. Among many promising organic semiconducting materials, pentacene has been a benchmark in this research field. Understanding the bottlenecks of carrier transport in pentacene OTFTs is therefore important to maximize the performance of OTFTs. In this paper, we summarize our knowledge on the bottlenecks against carrier transport in practical polycrystalline organic thin films: extrinsic factors that disturb the carrier transport in OTFTs, intrinsic structure and properties, equations to express the overall carrier mobility in polycrystalline films, and influence of surface chemical modification on the crystallographic and electronic structures.
Keywords: organic thin-film transistor, polycrystalline film, carrier mobility, band-edge fluctuation, crystallographic structure

1. Introduction

Pentacene is one of the most extensively studied semiconducting materials for organic thin-film transistors (OTFTs) and has been still a benchmark material in this research field. Although precise studies on the structure and electronic properties of pentacene single crystals give us exact knowledge about this material, there exists a large gap between the fundamental physics of single crystal and device characteristics brought by practical polycrystalline films. Understanding the bottlenecks of carrier transport in pentacene OTFT is therefore important to maximize the performance of OTFTs utilizing not only this benchmark material but also any semiconducting small molecules. In this paper, the reality of the carrier transport band in practical polycrystalline organic thin films is explained by making pentacene into a representative case, mainly based on our efforts of ten-years [1-7]. The major topics included are as follows: grain morphology and crystal structure of pentacene thin films, extrinsic factors that are more-or-less introduced and disturb the carrier transport in OTFTs, intrinsic structure and properties of pentacene polycrystalline thin films, equations to express the overall carrier mobility in polycrystalline films, and influence of surface chemical modification on the crystallographic and electronic structures.

2. Overview of the morphological features of pentacene thin films

Pentacene exhibits a relatively high mobility of >1 cm^2/Vs even for vacuum evaporated thin films [8-11]. Active layers of OTFTs are generally used in polycrystalline state and transistor characteristics are strongly influenced by the film morphology. Therefore, knowledge of the correlation between film morphology and electronic properties is important to improve device performance.

Morphology of pentacene crystalline grains is categorized into five groups [1]: “lamellar grains” of which height tends to be higher than surrounding other grains, “pyramidal grains” which are the most popular shapes having relatively symmetric shapes, “inclined grains” which are more asymmetric than the pyramidal grains, and “dendritic grains” which have a branching structure as frequently seen in diffusion limited growth. Grains with irregular shape more than 5 μm in size are named as “giant grains”. Figure 1 summarizes a phase diagram of the grain morphology against growth temperature and rate. Two overlapped markers indicate that the film is composed of two types of grains, a larger marker denotes a major component and a smaller a minor. The lamellar structure appears frequently when the growth temperature is less than 10°C. The dendritic region is isolated in the diagram, which would be related to the limited condition for

Received April 30, 2014
Accepted June 2, 2014

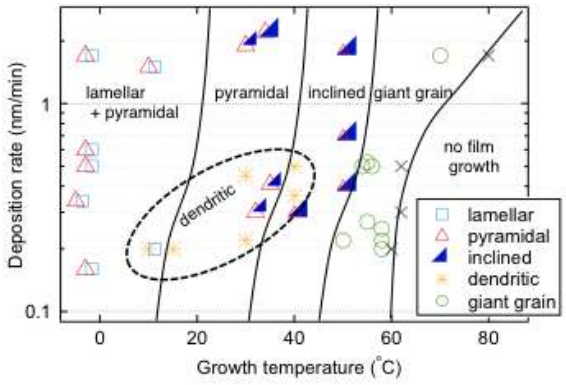

Fig. 1. Morphological phase diagram of pentacene films grown on SiO_2. The vertical axis indicates not a flux of incident but deposition rate.

supersaturation of migrating molecules [12].

Vacuum evaporated pentacene films are known to be composed of two crystalline phases, namely the "thin-film phase" and "bulk phase", and the ratio of the two phases varies depending on growth conditions [13]. The films consisting of thin-film phase generally exhibit higher mobility than those with a mixture of the two phases [14]. According to X-ray diffraction (XRD) measurements, all films analyzed in this work are highly ordered showing sharp diffraction peaks. On any growth conditions, a diffraction peak indicating 1.54 nm interplanar spacing is the strongest, which indicates that the major component of these films is the thin-film phase. Since only the films in which lamellar-like grains exhibit a diffraction peak of which interplanar spacing is 0.46 nm, the lamellar grains are concluded to be composed of "flat-lying molecules" [15, 16]. A peak corresponding to the bulk phase with a 1.45 nm interplanar spacing is observed above 35°C and gradually increased with increasing growth temperature. The bulk phase is, however, a minor component even near the growth limit. The intensity ratio between thin film and bulk phases are almost independent of the growth rate. The absence of the bulk phase is mainly because the thicknesses of the films are relatively thin, <50 nm.

3. Extrinsic limiting factors of carrier mobility in pentacene thin-film transistors

In many cases, top-contact thin-film transistors (TC-TFTs) tend to exhibit higher apparent mobility than bottom-contact thin-film transistors (BC-TFTs). The contact resistance at source/drain electrodes in the top-contact configuration is, in general, smaller or almost negligible for relatively large channel-length OTFTs. However, even the top contact configuration is sometimes accompanied with extrinsic degradation of the apparent mobility depending on the fabrication processes. The apparent field-effect mobilities calculated from the characteristics of TC-TFTs are, in many cases, smaller than the true field-effect mobilities [2]. Therefore, we have to be careful in analyzing the dependence of the apparent mobility on deposition conditions. Especially, the films having higher intrinsic mobilities suffer the electrode-originated degradation more.

Figures 2(a) and 2(b) show atomic-force-microscope potentiometry (AFMP) [3, 4, 17-19] images taken on a pentacene TC-TFT grown at relatively high temperature, 50°C. The applied drain and gate voltages correspond to the linear regime of the OTFT. The topographic and high-pass-filtered potential images indicate where the degradation has concentrated. In the potential image, potential drops are seen on certain parts of the grain boundaries encircled by dashed ovals. It seems difficult for carriers to flow straight without crossing these potential drops. A histogram of the

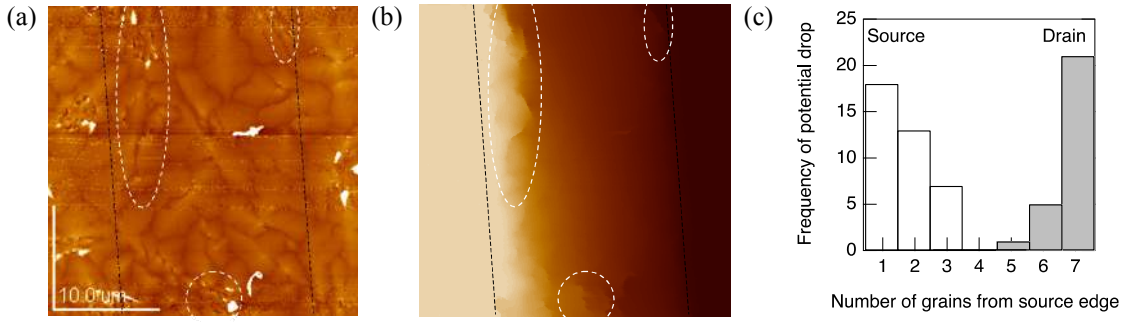

Fig. 2. 30×30 μm^2 AFMP images taken on a working pentacene TC-TFT (growth temperature: 50°C, growth rate: 0.31 nm/min): (a) topographic and (b) high-pass filtered potential images. A source electrode is located on the left side and a drain on the right side of each image (V_{DS} = –5 V and V_G = –30 V). (c) Histogram of the position of major potential drops (> 100 mV). The position is indicated by the number of grains from the source edge.

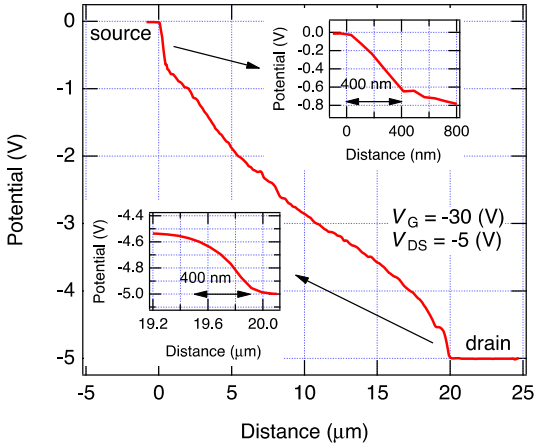

Fig. 3. Potential profile across the channel of a working pentacene TC-TFT (growth temperature: 15°C). Insets are magnified profiles at both ends of the channel.

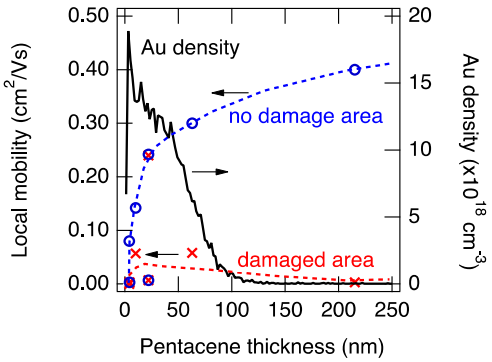

Fig. 4. Pentacene-thickness dependence of local mobilities in damaged (crosses) and no-damage (circles) areas. The pentacene films were grown with the same conditions as Fig. 3. Au depth profile measured by SIMS (solid line) is also plotted on right axis.

position of large potential drops was obtained from many similar images, shown in Fig. 2(c). The influence of the electrodes on the formation of potential drops is obvious from this distribution. Thus, the top contact causes serious electrical damage to the films grown at high temperatures, i.e. those with large grain sizes, because highly resistive grain boundaries are densely formed near the electrodes. This damage possibly reduces the apparent field-effect mobility to only 10-30% of the intrinsic one [2].

Such degradation is also seen when the growth temperature is relatively low. Figure 3 shows a potential profile through the channel region taken on a pentacene TC-TFT grown at a relatively low temperature, 15°C. Steeper potential slopes near the source and drain edges are clearly observed. The width of the steeper slope is around 400 nm equally on each side, which means that it is too wide and symmetric to be caused by an injection barrier. The width corresponded well to the area with a trace amount of Au incident on it, of which the amount is too small to be detected by AFM topographic images. The Au is supposed to be scattered by the edge of the shadow mask or residual gas during the vacuum evaporation. This steeper potential slope is therefore due to the electrical damage in pentacene induced by the trace amount of Au [18]. In this case, the apparent mobility was estimated to be about 75% of the intrinsic one.

Depth of the Au-induced electrical damage to the pentacene films deposited at higher temperature was investigated by changing the pentacene thickness. Figure 4 shows pentacene-thickness dependence of the local field-effect mobilities in the damaged and no-damage areas calculated from potential profiles under FET operation [2]. An Au depth profile measured by secondary ion mass spectrometry (SIMS) is also shown. According to the depth profile, Au penetrated approximately 100 nm into the pentacene layer. Such deep penetration would be mediated by the Au diffusion through grain boundaries, which has been confirmed by transmission electron microscopy for other organic polycrystalline films [20]. Since the output current flows at the pentacene/insulator interface, once the pentacene layer becomes thicker than the damaged layer, the local field-effect mobility is expected to increase. However, the low local mobility in the damaged area does not recover even when the pentacene thickness becomes much thicker than 100 nm. This result implies that the distribution of the electrical damage is deeper than that of the Au atoms themselves. One possible mechanism of the damage formation down to the bottom of the thick organic film is the transformation of the crystal structure. According to XRD analyses, the lattice plane distance decreased from 1.46 to 1.45 nm by Au deposition [2], which suggests that all of the pentacene molecules in the film have collectively inclined, i.e. became closer to the bulk phase. This transformation changes the molecular packing at the grain boundary from top to bottom of the film, and, as a result, makes the grain boundary more resistive due to the concentration of stress.

Another interesting fact seen in Figs. 2 and 3 is that no significant injection barrier is likely to exist at the source electrode/pentacene interface although a 0.85 eV barrier at the pentacene/Au interface is confirmed with electron spectroscopy [21]. The absence of the injection barrier may arise due to the

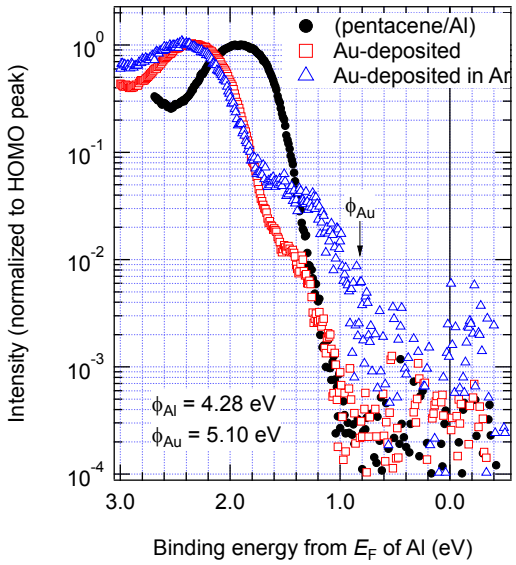

Fig. 5. Photoelectron spectra of pentacene/Al samples: (circle marks) without Au deposition, (square marks) with Au deposited in vacuum, and (triangle marks) with Au deposited in 0.2 Pa Ar.

carrier injection mechanism into the organic semiconductor with a large density of gap states mostly at grain boundaries, which is an advantage of the top-contact configuration. Figure 5 shows the influence of Au deposition on pentacene on the density-of-state (DOS) near the highest occupied molecular orbital (HOMO). These spectra were measured after the removal of the deposited Au layers from the pentacene films [22, 23]. By the Au deposition, the peak position of the pentacene HOMO shifts to the high binding energy side by ~0.5 eV. Moreover, another feature appears at approximately 1 eV above the HOMO level, demonstrating that the gap states appeared upon the Au deposition. The energy shift of the HOMO level can be elucidated by the Fermi-level pinning by the increased gap states [24, 25]. The density of the gap states in the pentacene with low-energy Au deposited in Ar is much greater than that with Au deposited in vacuum. This fact indicates that the gap state is not due to the heat damage of pentacene but due to the incorporation of Au atoms in the pentacene film.

The spatial distribution of the large ohmic current flowing vertically through Au deposited pentacene films was studied with AFM current imaging [22]. The ohmic current spots were concluded to be located at the grain boundaries by comparing topographic and current images. When the probe was biased positively, the forward thermionic current appears at several different points. The thermionic spots are located even in the grains. Accordingly, the two current components do not uniformly flow but are concentrated at different

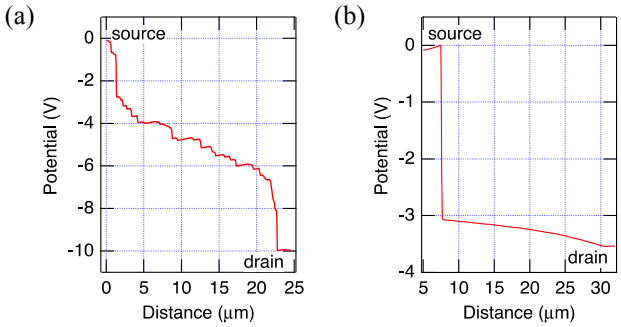

Fig. 6. Potential profiles of working BC-TFTs: (a) a pentacene OTFT with large contact resistance and (b) a CuPc OTFT with large injection barrier.

spots in the polycrystalline pentacene film. These images are instructive for study on metal/organic interfaces because they indicate that such singular spots possibly dominate the current conduction. On the other hand, many spectroscopic techniques measure averaged information over the entire film. This difference frequently causes the quantitative disagreement between the electrical and spectroscopic results [23].

In contrast to the small contact resistance of TC-TFTs, there frequently appears large contact resistance, or a carrier injection barrier, when the bottom-contact configuration is used. Figure 6(a) shows an example of the potential profile obtained on an inferior performance BC-TFT with a pentacene active layer. One can see abrupt potential slopes at both sides of the channel region of which width is approximately 1 μm. These are due to small crystal grains of which nucleation and growth is strongly influenced by the edge structure of the source/drain electrodes. In this case, approximately 2/3 of the applied V_{DS} is consumed at the narrow low mobility area near the source/drain electrodes. We have to note that this resistive area does not behave as a fixed resistance but as a very low mobility semiconductor. Since 10% of the channel length is filled with such a very low mobility semiconducting film, the apparent mobility becomes approximately 1/3 of the intrinsic one. This possibly appears as the V_G dependent "contact resistance" when transfer line method is used for BC-TFTs [26].

When there exists a large injection barrier at the electrode/organic interface, a large abrupt potential drop appears only on the source side as shown in Fig. 6(b). In this case, only 1/7 of the applied V_{DS} is used for the drift motion of the carriers in the channel region and the rest is consumed to inject the carriers from the source electrode. Furthermore, the effective gate electric field becomes much smaller than expected because the average channel

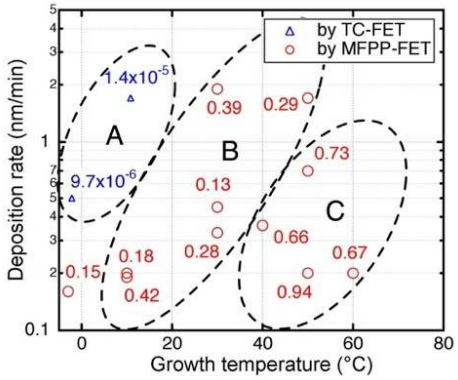

Fig. 7. Carrier mobilities in units of cm^2/Vs summarized in the plane of growth temperature and deposition rate. Numbers with triangle marks are the apparent mobilities measured by TC-TFT and those with circle marks by micro-four-point-probe (MFPP) FET].

potential is much closer to the negatively biased drain electrode, which results in poor accumulation of carriers and extremely low apparent field-effect mobility, 1/10 to 1/100 of the intrinsic value.

The problems originated in the source/drain electrodes discussed above are practically the major issue when the reproducibility of the device characteristics is poor and the insufficient characteristics are suspected to depend on the detail of the fabrication methods. In turn, one of the next major issues is the grain boundary of the organic layers. Dependence of the intrinsic field-effect mobility, which means that it does not contain the influence of the contact resistance, on the growth condition is summarized in Fig. 7. There is a general tendency that the carrier mobility becomes higher when the film is deposited at higher temperature and lower deposition rate, i.e. when the average grain size is larger. Here, we classify the films into A, B and C groups. From the standpoint of film morphology, group A is characterized by the frequent existence of the lamellar grains, where molecules lie flat against the substrate, and group B mainly contains the pyramidal or the dendritic grains. Group C is composed of the giant grains with many defective structures, such as cracks between grains and depressions in the grains. Not only the cracks in the film but also the lamellar grains are confirmed to behave as insulators by AFMP analyses [2]. Molecules lie flat in lamellar grains, while they are nearly perpendicular to the substrate in other types of grains. From this difference, the overlap of π-orbitals between the lamellar and other grains is much smaller than that between the grains with similar molecular orientations. Furthermore, standing orientation of rod-like π-conjugated molecules is generally suitable for OTFTs because it tends to mediate two-dimensional carrier transport via large transfer integrals between the nearest neighbors within the substrate plane. The apparent field-effect mobility is therefore strongly affected by the insertion of these insulating structures into the organic layers especially in group A.

4. Intrinsic limiting factors of carrier mobility in pentacene thin-film transistors

Figure 8 shows the intrinsic carrier mobility values plotted against the average diameter of pentacene grains. The mobility is similarly proportional to the grain size as several have reported [8, 15, 27], except in a sample with extremely large grains, 8 μm in average, grown near the growth limit conditions and containing a large amount of cracks. This implies that the mobility is dominantly limited by the grain boundaries.

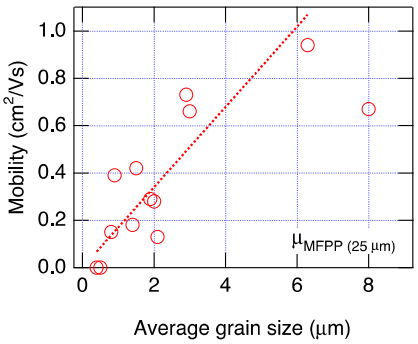

Fig. 8. Plot of carrier mobility obtained with MFPP-FET vs. average diameter of the grains. The probe spacing used was 25 μm.

Similar results have been obtained in the field-effect measurement of oligothiophene by Horowitz and Hajlaoui [27, 28]. They tried to analyze the property by a conventional "polycrystalline model" where carriers pass over back-to-back Schottky barriers, which are generated by traps at grain boundaries, via thermionic emission. Although the proportionality to the grain size was well explained by the polycrystalline model, the analysis was not so satisfactory because the calculated mean thermal velocity of carriers was too small as a thermal velocity. In the case of pentacene, the mean free path is almost equal to the molecular distance, and a typical Debye length of lightly doped pentacene films, e.g. those exposed to the air, is

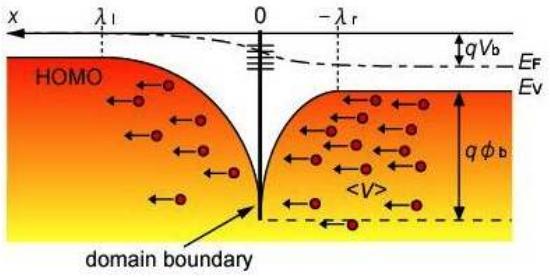

Fig. 9. Band diagram near a grain boundary used for the polycrystalline model with diffusion theory.

several tens of nanometers. Accordingly, application of the diffusion theory is more appropriate for the analysis of pentacene polycrystalline films. The band diagram used in the polycrystalline model with the diffusion theory is shown in Fig. 9. In this model, the externally applied drain-source voltage, V_{DS}, is divided by the number of grain boundaries, and thus $V_b=V_{DS}/(L/l)$, where L is the channel length and l the grain size, is applied to a single grain boundary. At a very low V_b condition, the apparent mobility for the boundary limited condition, μ_{BL}, is given by

$$\mu_{BL}=\frac{ql}{2k_BT}\mu_{di}\sqrt{\frac{qN_A\phi_b}{2\varepsilon_S}}\exp\left(-\frac{q\phi_b}{k_BT}\right), \qquad (1)$$

where q is the elementary charge, μ_{di} the mobility in the domain, N_A the acceptor density, ε_S the dielectric constant, ϕ_b the barrier height at the grain boundary, k_B the Boltzmann constant, and T the absolute temperature. Here, we used a term crystalline "domain" instead of grain. In some organic thin films, the morphological crystal grain, which is frequently determined by electron microscopy or AFM as a granular cluster, does not necessarily correspond to a single crystalline domain that is surrounded by large potential barriers against carrier transport. In the case of pentacene, the average domain size is known to be approximately half of the morphological grain size [3]. Eq. (1) is valid to express the apparent field effect mobility of an OTFT when the true drift mobility in the domain interior μ_{di} is relatively high and the grain boundary is resistive enough, where most of the applied drain–source voltage is distributed to the depletion region near the grain boundaries, as depicted in Fig. 9. From Eq. (1), one may notice that we should increase l and N_A, and decrease ϕ_b to increase the apparent mobility. The influence of N_A is due to the reduction of the depletion region width near the grain boundary, and it could be a considerable cause of the increase of apparent mobility by oxygen or other dopant species in relatively high mobility materials [29, 30].

According to the modified polycrystalline model and the domain size dependence of the mobility, the barrier height was independent of domain size and the average height estimated was approximately 150 mV. Similarly, μ_{DI} was also independent of domain size and the average value was approximately 1.0 cm^2/Vs. Let us compare this value with those in other reports. Field-effect mobility of 15–40 cm^2/Vs is reported for carefully fabricated pentacene single crystal FETs with organic gate insulators [31]. Over 10 cm^2/Vs mobility is also expected from the hole effective masses estimated from band calculation for single crystals [32] and angle-resolved ultraviolet photoemission spectroscopy against single-crystal-like monolayers on atomically flat substrates [33, 34]. These values are over ten times as large as that obtained in this work. This disagreement suggests the existence of another limiting factor of carrier transport in addition to the barriers at domain boundaries.

During AFMP observations of working OTFTs, we found that the crystal domains of pentacene commonly contain small potential fluctuations in addition to large potential drops at the domain boundaries. By careful experiments to eliminate the influence of topographic features from potential images, we concluded that the edge of the carrier-transporting band in a crystal domain, which was formerly thought as a single crystal, is not flat but randomly fluctuates with a few ten-nanometer periods [4]. We therefore converted the potential profile $V(x)$ taken by AFMP into band-edge profile $\varepsilon_v(x)$ by the following equation:

$$\ln\left[1/\left(dV(x)/dx\right)\right]kT=\left(\ln\frac{q\mu N_v}{J}kT-\varepsilon_f\right)+\varepsilon_v(x). \qquad (2)$$

where μ is the mobility, N_v the 2D effective density of states in the HOMO band, and ε_f the Fermi level.

Figure 10 shows the extracted band fluctuation in the domain. Here, the maximum amplitude within the domain must be much smaller than the barrier height of more than 100 meV at the domain boundaries. The maximum amplitude of 30 meV and the FWHM of 12 meV obtained in this study are consistent with this requirement.

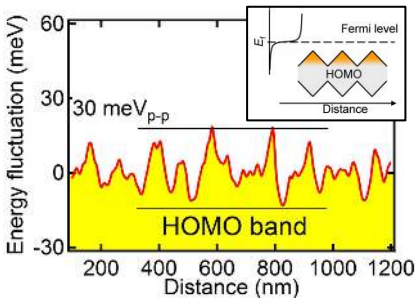

Fig. 10. Band diagram near a grain boundary used for the polycrystalline model with diffusion theory.

The band-edge fluctuation notably degrades the in-domain mobility μ_{DI} in Eq. (1). We propose two possible degradation mechanisms: (a) If the band fluctuation behaves as shallow traps, carrier transport within a domain follows a multiple-trapping and release mechanism, [35] and (b) if current flow meanders through the high-conductance region for small V_{DS}, carrier transport within the domain follows a percolation mechanism [36]. The conductance in a domain is proportional to the power of the space-filling factor in this case. According to the terahertz (THz)-wave absorption spectra by the accumulated holes [5], it is highly probable that the multiple-trapping and release mechanism dominantly determines the typical carrier transport phenomena in OTFTs. Either of these mechanisms results in the reduction of the mean carrier velocity in a domain. It thus appears as if μ_{DI} is much smaller than, approximately 1/10 at room temperature, that of perfect single crystals.

The potential fluctuation, of which root-mean-square amplitude is around 10 meV, is relatively small and may not be clearly noticed by most of spectroscopic analyses at room temperature. However, it strongly influences the carrier motion even in a short distance range. Figure 11 shows THz absorption spectra by gate-field-induced electrons in a single-crystal silicon (horizontally hatched area) and gate-field-induced holes in an OTFT-grade pentacene thin film (vertically hatched area) [5]. Although the spectral shape of the electron in silicon is well explained by the Drude model, which classically describes the dynamics of free electrons in solids, that of the holes in pentacene cannot. The absorption increases by increasing frequency from 0.5 to 2.0 THz, while a Drude-like tail appears at the low frequency end. The Drude component appears only after sufficiently high on-state gate voltage is applied.

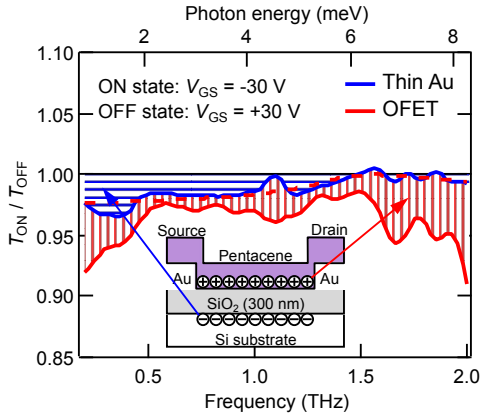

Fig. 11. Terahertz(THz)-wave modulation absorption spectra of a pentacene OTFT measured by time-domain spectroscopy. The red line indicates the absorption by the accumulated carriers in an OTFT and the blue line that of a control sample which is only sensitive to the carriers in the Si substrate. Dashed line is a theoretical curve obtained using the Drude model.

5. An integrated model to express the apparent carrier mobility in practical thin-film transistors

Here, we summarize a model to account for the apparent and 'intrinsic' carrier mobility in practical OTFTs where polycrystalline films are used as active layers. Here, the word 'intrinsic' does not mean that the semiconductor layer is a perfect single crystal but that the overall carrier mobility is not influenced by many extrinsic limiting factors that are explained in Section 3. Although this model is derived from the experimental results on pentacene thin films grown on SiO_2 substrate, it could be universally used for most of high-mobility organic polycrystalline thin films.

When the resistance of the domain boundary is high enough to consume almost all of the applied drain–source voltage, the boundary-limited mobility is well explained by the modified polycrystalline model with diffusion theory and is expressed by Eq. (1). Then, μ_{DI} is not the one obtained in the single crystal and notably reduced by the potential fluctuation in the domain. Potential distribution of the fluctuated band edge can also be regarded as an exponential distribution of the tail state of which decay energy is around 10 meV [4]. The influence of such a tail state on carrier transport is well studied for inorganic amorphous semiconductors, e.g. a-Si or a-Ge, where the gap-state distribution is frequently referred as an "Urbach tail". Various models have been proposed to precisely explain the carrier transport in amorphous semiconductors.

There exists however a quantitative difference between the tail states in inorganic semiconductors and pentacene. The decay energy of the inorganic tail states is two to three times larger than that of pentacene and, furthermore, their spatial period of band-edge fluctuation is much shorter than carrier mean free path in contrast to the much longer period in pentacene. The "detrapping and drift" phenomenon in pentacene crystal domain is therefore expected to be much closer to a simple thermally activated process. Nevertheless, as long as the temperature dependence is noted, Arrhenius-like temperature dependence is observed for both inorganic [37] and organic [38] semiconductors. We therefore assume that the mobility in domain interior can be simply expressed by

$$\mu_{\mathrm{DI}} = \mu_0 \exp\left(-\frac{q\phi_{\mathrm{f}}}{k_{\mathrm{B}}T}\right), \tag{3}$$

where μ_0 can be now regarded as the mobility in a single crystal and ϕ_{f} the mean barrier height in the fluctuating band. The temperature dependences of Eqs. (1) and (3) are slightly different due to the pre-exponential factors in Eq. (1). It would however be difficult to separate these parameters, ϕ_{b} and ϕ_{f}, only by the temperature dependence of apparent mobility, if they are close to each other.

When the voltage consumption by the domain interior is not negligible, we have to consider the series connection of the two equivalent registers: total resistance of the part where the carrier mobility is limited by the domain boundary, and that limited by the band-edge fluctuation. The overall mobility of such a polycrystalline film is now expressed by

$$\frac{1}{\mu} = \frac{\alpha}{\mu_{\mathrm{BL}}} + \frac{1-\alpha}{\mu_{\mathrm{DI}}}, \tag{4}$$

where α is the ratio between the total length of the domain boundary region and the channel length.

6. Overview of band-edge and crystallographic structures in pentacene thin films

Now, the biggest question remained is the origin of the band-edge fluctuation within a crystal domain. There are two possible origins:

(1) The crystalline domain itself is a single crystal but contains random strains, or
(2) The crystalline domain is a mosaic of smaller crystallites and potential fluctuations are generated due to the crystallite boundaries.

We therefore determined the structural origin by using glazing-incidence X-ray diffraction (GIXD) analyses with synchrotron radiation source [6].

In general, the peak widths of XRD patterns are broadened not only by the size of crystallite but also by the random strain in the crystal structure. The Williamson–Hall (W–H) method can separate these two factors from the widths of the XRD peaks [39]. In this method, the relation between these structural parameters and peak width is described as follows:

$$\beta_{\mathrm{q}} = \frac{2\pi K_{\mathrm{S}}}{\langle D \rangle} + \varepsilon_{\mathrm{rms}} q_{\mathrm{xy}}, \tag{5}$$

where β_{q} is the FWHM of a peak, K_{S} the Scherrer constant, $<D>$ the average crystallite size, $\varepsilon_{\mathrm{rms}}$ root mean square of the random strain, and q_{xy} the scattering vector. In this work, we adopt K_{S}=0.95 which is in the middle of the range used for organic crystals, 0.87–1.05 [40–43].

Figure 12(a) shows the W–H plots of major diffraction peaks obtained with pentacene thin films [6]. It is to be noted that no sample has a clear positive slope in its W-H plot. This result indicates that the FWHMs of the X-ray diffraction peaks from the pentacene films are determined by their finite crystallite sizes and the contribution of random strain is negligible. Therefore, hereafter, we only discuss the crystallite size estimated for each peak by the Scherrer equation, which only contains the first term in Eq. (5). In Fig. 12(b), the crystallite size calculated from each peak is plotted against the crystal domain size of the film. Although crystal domain size is varied more than ten times by changing the growth temperature, surprisingly, the crystallite size is unchanged. The estimated crystallite size is within the range of 25–50 nm and one- to two-orders-of-magnitude smaller than the domain size. By analyzing the characteristic frequency of the band-edge fluctuation, we found that the fluctuation period agreed with the crystallite size. Thus, we concluded that the band-edge fluctuation is caused by the small mosaic structure within the crystal domain.

Figure 13 schematically summarizes the energy diagram and film structure of a pentacene polycrystalline film. A pentacene polycrystalline film consists of hierarchical structures, including (i) the micrometer-scale morphological grain, (ii) the polycrystalline domain surrounded by large energy barriers for carrier transport, (iii) the ten-nanometer-scale crystallite, (iv) the unit cell of the crystal, and (v) the molecule. A morphological grain of pentacene on SiO_2 has its nucleus at

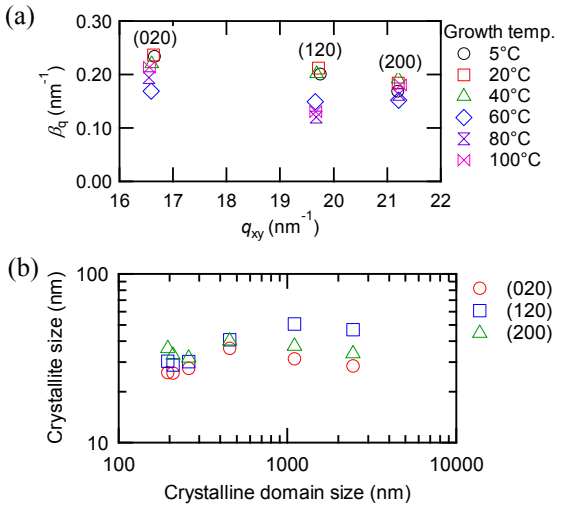

Fig. 12. (a) Williamson–Hall plot of the major GIXD peaks obtained with pentacene thin films grown at 5, 20, 40, 60, 80, and 100°C. (b) Relationship between crystallite size estimated using the Scherrer equation and the polycrystalline domain size of the pentacene film.

around the center and four branches grow from the nucleus toward four directions. Each branch finally becomes the crystalline domain (ii). During film growth, the branches coalesce so as to form, in most cases, a smooth pyramid-shaped morphological grain (i) and the boundary of (ii) is invisible in an AFM image. The boundaries of (i) and (ii) are however almost equivalent and crucial limiting factors for carrier transport because their barrier height is more than 100 meV. Moreover, (ii) is still not a single crystal and the boundary of (iii) introduces 10-meV-scale fluctuations of the band edge. The barrier height at the boundary of (ii) is much higher than that of (iii) because crystal orientations are more different between two neighboring domains than between connected crystallites due to the different orientation of triclinic crystals.

As shown in Fig. 8, overall apparent carrier mobility is often proportional to the grain size. Many researchers therefore attempt to maximize the grain size or to grow single crystals on the substrates. This approach is effective when the largest limiting factor is the boundary of (ii). However, when the crystal contains high-density defects as in the pentacene films, the largest bottleneck is (iii) because the apparent mobility is always proportional to the in-domain mobility as in Eq. (1). Since the crystallite size is mainly determined by defect formation during the film growth on an atomically rough substrate [6], a limited way to escape from this bottleneck is the use of single crystal grown in a free space or in a solution. Although chemical composition is known to influence on the overall mobility [8, 9, 15], we have found that the improvement of mobility is only due to the increase of domain size [7].

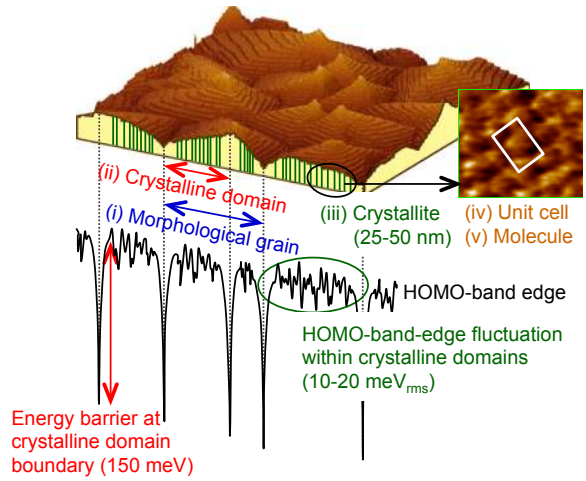

Fig. 13. Schematic illustration showing (top) crystallographic and (bottom) HOMO-band-edge structure in a pentacene polycrystalline film.

7. Conclusion

In this paper, we strived to elucidate all of the extrinsic and intrinsic limiting factors of carrier mobility in organic polycrystalline films according to our comprehensive study on pentacene thin films. We can find thousands of papers that discuss parts of this issue. However, as long as we compare imperfect OTFTs fabricated by different techniques and conditions, the argument will never reach a consensus. This is the reason why we have paid continuous efforts to investigate all extrinsic and intrinsic factors using the OTFTs similarly fabricated with the same material, techniques, and conditions. As a result, we believe that the mobility limiting factors in pentacene OTFTs are almost completely classified and quantitatively understood. Physical or chemical origins of some of the limiting factors, e.g. physical origin of the bad-edge fluctuation, chemical origin of the traps at the domain boundary inducing carrier depletion, etc., are still open questions. Nevertheless, the knowledge and methodology in this series of works should be generally applicable to any polycrystalline OTFTs.

Acknowledgements

The works in this paper were supported in part

by the Full Color Rewritable Paper Project (NEDO), the Chiba University 21st Century COE Program “Frontiers of Super-Functionality Organic Devices”, the Chiba University Global COE Program “Advanced School for Organic Electronics”, Grant-in-Aid for Scientific Research (No. 21350099 and 23655171), a Grant-in-Aid for JSPS Fellows (No. 23-56142) (MEXT), and the NAIST Green Photonics Research Project (MEXT).

Reference

1) H. Yanagisawa, T. Tamaki, M. Nakamura, and K. Kudo, *Thin Solid Films*, **464-465** (2004) 398.
2) M. Nakamura, H. Ohguri, N. Goto, H. Tomii, M.-S. Xu, T. Miyamoto, R. Matsubara, N. Ohashi, M. Sakai, and K. Kudo, *Appl. Phys. A*, **95** (2009) 73.
3) R. Matsubara, N. Ohashi, M. Sakai, K. Kudo, and M. Nakamura, *Appl. Phys. Lett.*, **92** (2008) 242108.
4) N. Ohashi, H. Tomii, R. Matsubara, M. Sakai, K. Kudo, and M. Nakamura, *Appl. Phys. Lett.*, **91** (2007) 162105.
5) S.-G. Li, R. Matsubara, T. Matsusue, M. Sakai, K. Kudo, and M. Nakamura, *Org. Electron.*, **14** (2013) 1157.
6) R. Matsubara, M. Sakai, K. Kudo, N. Yoshimoto, I. Hirosawa, and M. Nakamura, *Org. Electron.*, **12** (2011) 195.
7) R. Matsubara and M. Nakamura, (in preparation).
8) D. Knipp, R. A. Street, A. Volkel, and J. Ho, *J. Appl. Phys.*, **93** (2003) 347.
9) H. Klauk, M. Halik, U. Zschieschang, G. Schmid, W. Radlik, and W. Weber, *J. Appl. Phys.*, **92** (2002) 5259.
10) R. Schroeder, L. A. Majewski, and M. Grell, *Appl. Phys. Lett.*, **83**, (2003) 3201.
11) D. Knipp, R. A. Street, B. Krusor, R. Apte, and J. Ho, *J. Non-Cry. Sol.*, **299** (2002) 1042.
12) U. Nakaya, *“Snow Crystals, Natural and Artificial”*, Harvard Univ. Press, Cambridge, (1954).
13) I. P. M. Bouchoms, W.A. Schoonveld , J. Vrijmoeth, and T.M. Klapwijk, *Synth. Met.*, **104** (1999) 175.
14) C.D. Dimitrakopoulos, A. R. Brown, and A.Pomp, *J. Appl. Phys.*, **80** (1996) 2501.
15) M. Shtein, J. Mapel, J. B. Benziger, and S. R. Forrest, *Appl. Phys. Lett.*, **81**, (2002) 268.
16) J. H. Kang and X.-Y. Zhu, *Appl. Phys. Lett.*, **82** (2003) 3248.
17) M. Nakamura, M. Fukuyo, E. Wakata, M. Iizuka, K. Kudo, and K. Tanaka, *Synth. Met.*, **137** (2003) 887.
18) M. Nakamura, N. Goto, N. Ohashi, M. Sakai, and K. Kudo, *Appl. Phys. Lett.*, **86** (2005) 122112.
19) M.-S. Xu, A. Ohno, S. Aramaki, K. Kudo, and M. Nakamura, *Org. Electron.*, **9** (2008) 439.
20) K. Suemori, M. Yokoyama, and M. Hiramoto, *J. Appl. Phys.*, **99** (2006) 036109.
21) N. Koch, A. Kahn, J. Ghijsen, J.-J. Pireaux, J. Schwartz, R.L. Johnson, and A. Elschner, *Appl. Phys. Lett.*, **82** (2003) 70.
22) T. Sawabe, K. Okamura, T. Miyamoto, T. Sueyoshi, N. Ueno, K. Kudo, and M. Nakamura, *Appl. Phys. A*, **95** (2009) 225.
23) T. Sugiyama, T. Sasaki, S. Kera, N. Ueno, and T. Munakata, *Appl. Phys. Lett.*, **89** (2006) 202116.
24) S. Yogev, R. Matsubara, M. Nakamura, U. Zschieschang, H. Klauk, and Y. Rosenwaks, *Phys. Rev. Lett.*, **110** (2013) 036803.
25) F. Bussolotti, J. Yang, A. Hinderhofer, Y. Huang, W. Chen, S. Kera, A.T.S. Wee, and N. Ueno, *Phys. Rev. B*, **89** (2014) 115319.
26) C. Vanoni, S. Tsujino, and T.A. Jung, *Appl. Phys. Lett.*, **90** (2007) 193119.
27) G. Horowitz and M. E. Hajlaoui, *Adv. Mater.*, **12**, (2000) 1046.
28) G. Horowitz, M. E. Hajlaoui, and R. Hajlaoui, *J. Appl. Phys.*, **87** (2000) 4456.
29) X.-J. Yan, H. Wang, and D.-H. Yan, *Thin Solid Films*, **515** (2006) 2655.
30) S. Verlaak, V. Arkhipov, and P. Heremans, *Appl. Phys. Lett.*, **82** (2003) 745.
31) O.D. Jurchescu, M. Popinciuc, B.J. van Weeks, and T. T. M. Palstra, *Adv. Mater.*, **19** (2007) 688.
32) K. Hummer and C. Ambrosch-Draxl, *Phys. Rev. B*, **72** (2005) 205205.
33) H. Kakuta, T. Hirahata, I. Matsuda, T. Nagao, S. Hasegawa, N. Ueno, and K. Sakamoto, *Phys. Rev. Lett.*, **98** (2007) 247601.
34) H. Yamane, E. Kawabe. D. Yoshimura, R. Sumii, K. Kanai, Y. Ouchi, N. Ueno, and K. Seki, *Phys. Stat. Sol. (b)*, **245** (2008) 793.
35) G. le Comber and W.E. Spear, *Phys. Rev. Lett.*, **25** (1970) 509.
36) D. Stauffer and A. Aharony, *“Introduction to percolation theory, Rev. 2nd ed.”,* Taylor & Francis, London (1994).
37) Q. Wang, H. Antoniadis, and E.A. Schiff, *Phys. Rev. B*, **47** (1993) 9435.
38) M.C.J.M. Vissenberg and M. Matters, *Phys. Rev. B*, **57** (1998) 12964.
39) G.K. Williamson and W.H. Hall, *Acta Metall.*, **1** (1953) 22.
40) R. Hussain and D. Mohammad, Turk. *J. Chem.*, **28** (2004) 725.
41) Y. Iwanami, H. Kamiishi, K. Matsuura, A. Sano, and S. Yokoyama, US Patent, 5002714 (1991).
42) H.S. Soliman, M.M. El Nahass, A.M. Farid, A.A.M. Farag, and A.A. El Shazly, *Eur. Phys. J. Appl. Phys.*, **21** (2003) 187.
43) F.Y. Tsai, T.N. Blanton, D.R. Harding, and S.H. Chen, *J. Appl. Phys.*, **93** (2003) 3760.